Intelligent and Sustainable Manufacturing

SciEPublish

Article

Stretchable Copper Micropatterns Embedded in Polydimethylsiloxane for Soft Wearable Devices

Manoj Singh Yadav [1], Nipun Singh [2], Ashutosh Vishwakarma [2] and Vijay Kumar Pal [1,*]

[1] Department of Mechanical Engineering, Indian Institute of Technology Jammu, Jammu 181221, India; 2022rme2020@iitjammu.ac.in (M.S.Y.)

[2] Department of Computer Science and Engineering, Indian Institute of Technology Jammu, Jammu 181221, India; 2022ucs0099@iitjammu.ac.in (N.S.); 2022ucs0083@iitjammu.ac.in (A.V.)

* Corresponding author. E-mail: vijay.pal@iitjammu.ac.in (V.K.P.)

Received: 23 July 2026; Revised: 7 August 2026; Accepted: 6 November 2026; Available online: 24 November 2026

ABSTRACT: Wearable devices worn directly on the body, for monitoring human motion, sensing as soft robotic skin, and health diagnostics, need conductive traces that stay connected and keep the signal stable when they are stretched or bent. First, micrometer-scale metal traces are hard to pattern on a soft substrate because conventional tools are designed for rigid wafers, and the substrate deforms during processing. Secondly, to address this, we patterned 36 μm copper foil laminated on the biocompatible elastomer polydimethylsiloxane (PDMS) by ultraviolet (UV) photolithography, using a dry film negative photoresist and maskless exposure at 365 nm. The exposure dose, the sodium carbonate developer concentration, and the ferric chloride etchant concentration were adjusted for each feature width, and the horseshoe-shaped traces were embedded by casting a second PDMS layer. Thirdly, qualitatively, a finite-element model showed that the adhesive under a 250 μm trace stays in compression up to 30% strain, whereas under a 1 mm trace it is pulled open, and that embedding reduces the out-of-plane deflection of the copper about fourfold. Furthermore, quantitatively, the process gave copper interconnects with a minimum linewidth of 250 μm and a thickness of 36 μm, and in a cyclic stretching test the embedded horseshoe interconnects kept the baseline of a strain sensor stable (a 7% relaxation, then a slow drift of about +0.02% per cycle, against +25% with straight copper leads) and made its response more linear and less hysteretic. Finally, the route needs no vacuum deposition, transfer step, or cleanroom.

Keywords: Photolithography; Stretchable substrate; Microfabrication of copper interconnects; Dry film negative photoresist; Etching; Stretchable electronics

1. Introduction

The application of miniaturized wearable devices on stretchable and flexible substrates has gained significant attention in recent years [1,2]. These emerging technologies demand materials and devices that bend, twist, stretch, and conform to complex geometries without losing electrical or mechanical functionality [3–5]. Such capabilities are crucial for flexible sensors, soft robotics, and skin-like electronics

© 2026 The authors. This is an open access article under the Creative Commons Attribution 4.0 International License (https://creativecommons.org/licenses/by/4.0/).

applications that adapt to human motion and dynamic environmental conditions [6,7]. Despite their potential, the fabrication of conductive micro- and nanoscale patterns on stretchable substrates remains challenging [8,9]. The interaction between mechanical strain and nanoscale material behaviour significantly influences the reliability and performance of these devices [10,11]. The high surface-area-to-volume ratio at these scales increases susceptibility to delamination, cracking, and microstructural distortion, often caused by mismatches in Young's modulus between elastomeric substrates (polydimethylsiloxane, PDMS) and conductive materials (copper). Additionally, pattern reliability is limited by alignment inaccuracies, thermal expansion mismatches during processing, and the difficulty of maintaining feature integrity under mechanical deformation [12,13]. Conventional fabrication processes often overlook these multiscale mechanical, thermal, and electrical interactions, creating a critical research gap in developing defect-tolerant manufacturing techniques for stretchable electronics. Achieving high conductivity and transparency in electrodes while minimising hysteresis effects remains an essential target [14,15]. Furthermore, the stretchability of substrates can cause deformation or warping during pattern formation, making precise microfabrication increasingly complex. Photolithography has emerged as one of the most reliable and accurate patterning techniques for such applications [16,17]. It allows the controlled transfer of micro- and nanoscale geometric designs onto photoresist-coated surfaces through exposure to ultraviolet (UV) light [18]. Based on surface relief structures in photoresists, photolithography enables accurate pattern formation and subsequent etching to create interconnects and electrodes on flexible substrates [19,20].

However, fabrication failures can still occur due to several process-related factors. Key parameters such as light exposure intensity, depth of focus (DOF), and etching conditions play critical roles in determining the quality and reliability of the patterned structures. For dry film negative photoresists (DFNPR), defects such as poor adhesion or contamination can cause incomplete or defective pattern formation. Insufficient adhesion between the photoresist and the copper substrate can lead to pattern delamination, while surface contaminants may introduce bubbles, undercuts, or irregular connections. An exposure dose of 100–180 mJ/cm^2, increasing with the width of the features, is required to properly crosslink and harden the negative photoresist. The photoresist remains underexposed when the exposure dose is too low for the feature width, leading to poor adhesion and pattern definition. During development, the unexposed regions are dissolved in a sodium carbonate (Na_2CO_3) solution prepared with deionised (DI) water, while the exposed areas remain intact to define the desired pattern. Additionally, depth of focus issues may arise due to variations in photoresist thickness or surface topography, leading to inaccurate pattern transfer. In this work, the resist is exposed at 365 nm (i-line). Post-lithography, the etching process further influences device reliability. The use of ferric chloride ($FeCl_3$) at a concentration of 10–20% in deionised water is typical for copper patterning. If etching parameters such as temperature, immersion time, and concentration are not tightly controlled, uneven or partial etching can occur, resulting in incomplete or defective patterns.

Stretchable interconnects on elastomers are commonly made from thin metal films (sub-micrometre gold or copper) evaporated or sputtered onto PDMS and patterned by photolithography, lift-off, or laser processing [5,21–23], or fabricated on a rigid wafer and transferred onto the elastomer [24,25]. These routes require vacuum deposition and usually a cleanroom or a transfer step, and the thin films limit the current-carrying capacity. Printed conductors (silver–elastomer composites or liquid metals) avoid vacuum processing but are less conductive than bulk copper or require a liquid to be contained [26,27]. Thick copper foil can be patterned into horseshoe-shaped meanders by adapting printed-circuit-board (PCB) processes [28,29]: in the stretchable moulded interconnect (SMI) process, the foil is etched on a temporary rigid carrier, moulded in PDMS and released, and in the stretchable circuit board (SCB) process, it is etched on a laminated polyurethane carrier [30]. Encapsulating such horseshoe and sine-wave interconnects in PDMS, and grading the stiffness of the substrate, changes how they deform and where they fail [31,32]. In the present route (Table 1), commercial 36 μm copper foil is laminated directly onto cured PDMS and patterned

in place with DFNPR and maskless exposure, without vacuum deposition, a carrier, a release step, or a cleanroom, and embedded by casting a second PDMS layer.

This study investigates how critical parameters, especially light exposure dose, DOF control, and etching conditions, affect the quality of photolithographic patterned structures on stretchable substrates [33]. This work establishes the process windows of these parameters, uses a finite-element model to choose the trace width and to assess the effect of embedding, and compares strain sensors with and without the embedded interconnects under cyclic stretching.

Table 1. Comparison of fabrication routes for stretchable interconnects on elastomers. Au is gold, Cu is copper, Ag is silver, and PU is polyurethane.

Route	Conductor	Vacuum	Carrier	Clean-Room	Refs.
Thin film on PDMS	Au/Cu, sub-μm	Yes	No	Usually	[21–23]
Transfer printing	Films, Si ribbons	Yes	Yes	Yes	[24,25]
PCB-based SMI	Cu foil	No	Yes	No	[28,30]
PCB-based SCB	Cu foil on PU	No	No	No	[30]
Printed	Ag ink, liquid metal	No	No	No	[26,27]
This work	36 μm Cu foil on PDMS	No	No	No	–

2. Experimental Section

2.1. Fabrication of Interconnects

In the experimental section, the PDMS-based flexible microfabricated sensor is fabricated using dry film negative photoresist (DFNPR) [34–36]. The process involves four main steps, as shown in Figure 1. The substrate is prepared with a uniform, thin, flexible layer of PDMS (Sylgard 184, Dow Silicones Corporation, Midland, MI, USA; 10:1, 0.5 to 1 mm) with a spin coater (WS-650 Series, Laurell Technologies, North Wales, PA, USA; 200 rpm, 50 s), cured in an oven (Thermo Fisher Scientific, Waltham, MA, USA) at 100 °C for 40–50 min (Figure 1a). Figure 1b shows copper tape's application on the cured stretchable substrate (3M 1125, 3M, St. Paul, MN, USA: 36 μm copper with a 31 μm acrylic adhesive), and then the application of DFNPR (Ordyl Alpha 350, Elga Europe, Milan, Italy) above the copper surface. When the DFNPR was applied, some tiny bubbles appeared on the copper surface, where the incident UV light could not harden the resist effectively, so the bubbles were removed, and the resist was bonded to the copper surface on a hot plate at 100–150 °C for 2–3 min to adhere better, without bubbles. The resist was exposed by maskless direct writing (ML3, Durham Magneto Optics, Caithness, UK; 365 nm, 5 lens) at 180 mJ/cm^2, which took 20 min per device; no cleanroom was used. The exposed pattern was developed in Na_2CO_3 (4 wt%, 5 min), and the copper was wet-etched in $FeCl_3$ (15%, 40 min), as shown in Figure 1b,c. This patterning method gives good control of the dimensions and keeps the patterned metal interconnects attached to the elastic substrate. After this, the metallization step was avoided because the DFNPR was already on the metal surface with a high aspect ratio compared to positive photoresist [37,38]. As shown in Figure 1d, after the etching process, a sensing composite was deposited onto the electrode region. Finally, the patterned structure was embedded by casting a second PDMS layer.

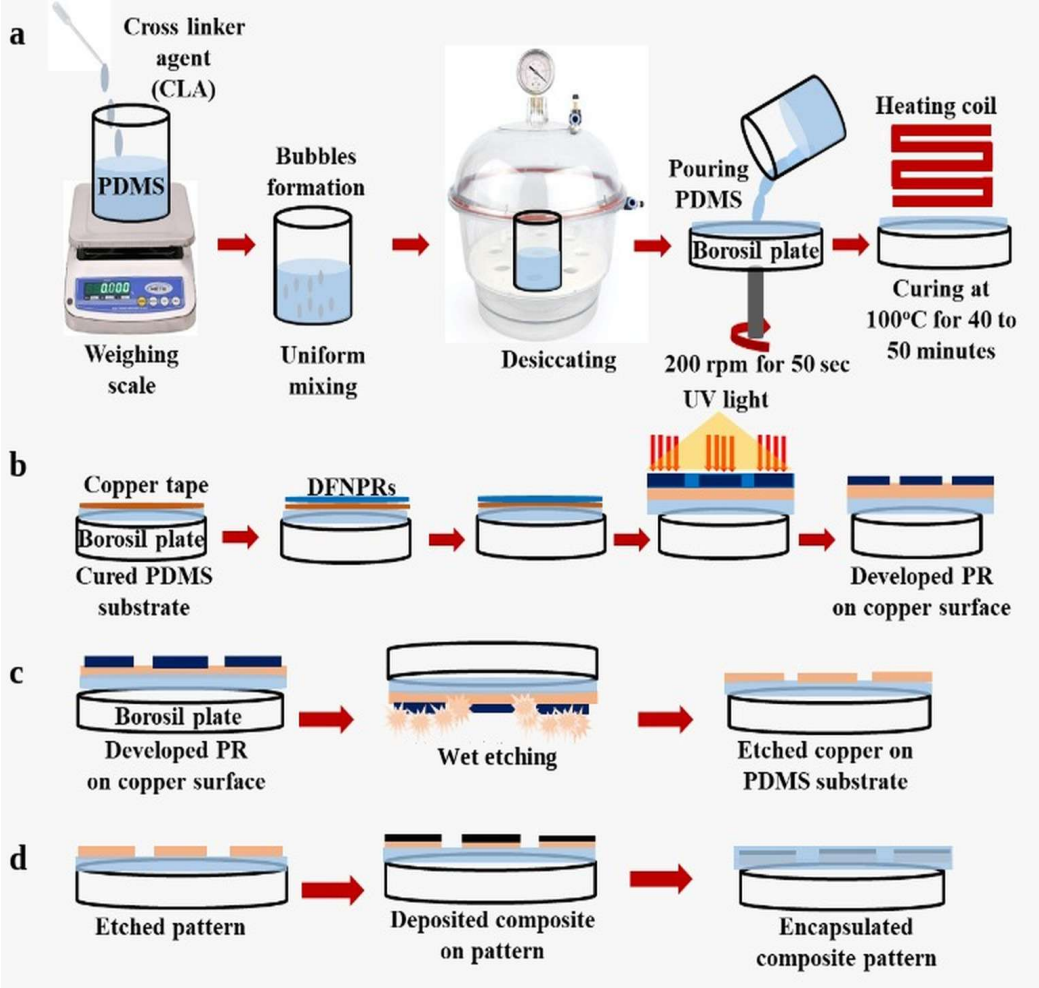

Figure 1. Schematic diagram of the fabrication process: (**a**) preparation of the PDMS substrate by mixing, degassing, spin-coating, and curing to obtain a uniform elastic layer, (**b**) photolithography, where a copper layer is laminated, coated with DFNPR, UV-exposed by maskless writing, and developed, (**c**) wet etching uses the developed photoresist as a mask to selectively remove exposed copper and form the conductive patterns, (**d**) the sensing composite is deposited, and a thin PDMS layer is applied and cured to encapsulate, embed, and finalise the sensor structure.

2.2. Sensing Composite and Electromechanical Testing

The composite was PDMS (10:1) with 1 wt% multi-walled carbon nanotubes (Sigma-Aldrich, St. Louis, MO, USA; ≥95% C, 10–20 nm diameter) and 1 wt% few-layer graphene nanoplatelets (Sigma-Aldrich, St. Louis, MO, USA; 3–10 layers, 1–5 µm, ≥99% C), mixed with n-hexane and ultrasonicated for 6 h, applied over the electrode fingers through a 0.5 mm stencil and cured at 150 °C for 30–45 min; the n-hexane was evaporated before encapsulation. A reference sensor used straight strips of the same copper foil instead of horseshoe interconnects (Figure 2). The samples were stretched in a custom machine (stepper-motor stage, 5 kg load cell (Honeywell, Charlotte, NC, USA), polylactic acid (PLA) grips printed on a Creality Ender printer (Shenzhen, China), 25 mm gauge length) at about 0.9 mm/s, with the same crosshead displacement (up to about 4.6 mm) for both sensors, while a Keithley 2110 multimeter (Keithley Instruments, Cleveland, OH, USA) measured the resistance in two-wire mode; extension, force, and resistance were logged at 100 Hz with an Arduino Mega 2560 (Arduino, Monza, Italy). Strain is referred to the length of the composite patch (11.3 mm with interconnects, 13 mm with straight leads). For each cycle, the baseline resistance R_0 (minimum strain), the gauge factor (slope of R/R_0 against strain), its linearity (R^2), and the hysteresis (largest loading–unloading difference relative to the span) were computed; cycles 1–3 are treated as conditioning.

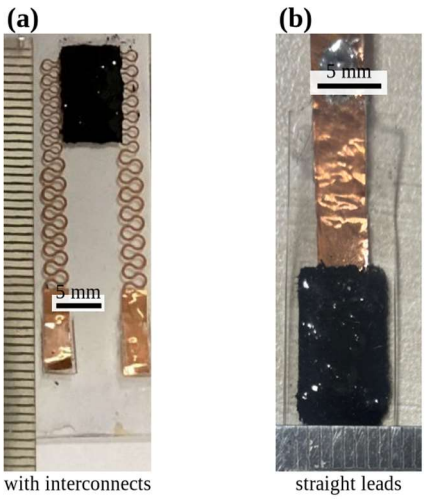

Figure 2. The two sensors: (**a**) with horseshoe interconnects and (**b**) with straight copper leads, photographed next to a ruler (scale bars from the ruler).

2.3. Finite-Element Model

One horseshoe period (Figure 3) was modelled in three dimensions in CalculiX 2.23 with large deformation: 1 mm PDMS, the 31 µm adhesive, the 36 µm copper trace, and 1 mm top PDMS. Copper was elastic–plastic (annealed, yield 70 MPa, hardening to 300 MPa); PDMS (E = 1.8 MPa, ν = 0.49) and the adhesive (shear modulus 0.1 MPa, assumed) were neo-Hookean. The 250 µm trace of the devices (period 1.9 mm) was compared with a 1 mm trace of the same shape scaled four times, and an embedded trace with one without top PDMS. The peel (through-thickness) and shear strains of the adhesive under the trace (95th percentile) indicate the tendency to delaminate, as the shear strain at the interface of encapsulated horseshoe interconnects matches the observed sites of delamination [31]; debonding itself is not modelled.

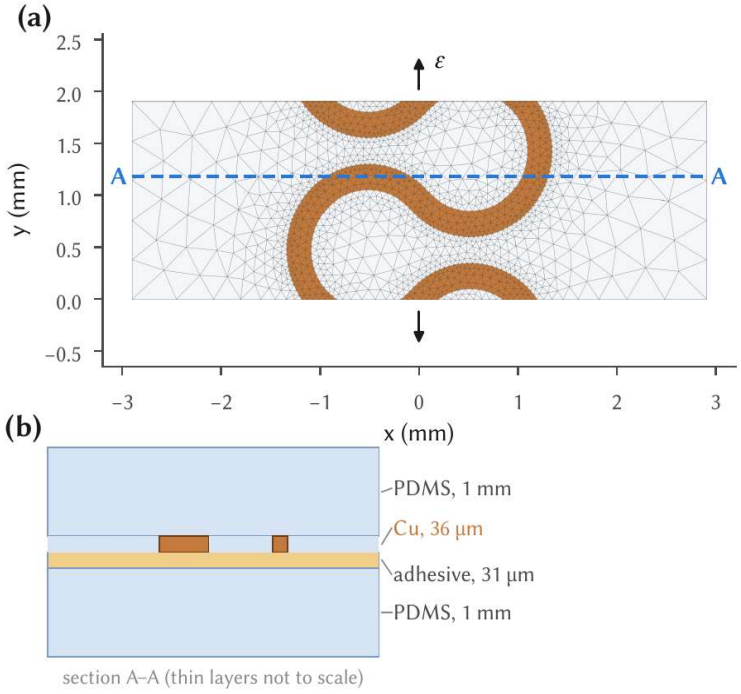

Figure 3. Finite-element model of one horseshoe period: (**a**) mesh of the copper trace (brown) and the surrounding PDMS, top view, stretched along y; (**b**) section A–A through the layer stack.

3. Result and Discussion

The DFNPR and $FeCl_3$ etching process was tuned to achieve reproducible microfabrication for sensor devices. As shown in Table 2, the exposure and development conditions depend on the width of the features: at a thickness of 36 µm, features up to 85 µm were developed after 100–120 mJ/cm^2 at 365 nm and 3 min in 2% Na_2CO_3, and features of 150 µm and wider after 180 mJ/cm^2 and 4–5 min in 3–4% Na_2CO_3. A soft bake at 100–150 °C for 2–3 min improved the adhesion of the resist on copper. Wet etching using $FeCl_3$ (15%) at 35–40 °C for 40 min resulted in uniform copper patterning, with no breaks or bridging of the traces in the samples shown. Two quality metrics were used: the peel and shear loading of the adhesive (finite-element model, Section 3.5), which set the trace width of 250 µm, and the stability of the resistance of a sensor built on the embedded electrodes under cyclic stretching (Section 3.6). The conditions that reproduced the 250 µm features were then selected.

Table 2. Process Parameters and Outcomes for DFNPR and Copper Etching.

Process	Parameter	Typical Range	Devices
Photoresist	Feature width	50–350 µm	250 µm
Exposure	Wavelength	365 nm UV	365 nm
	Dose	100–180 mJ/cm^2	180 mJ/cm^2
Development	Na_2CO_3 in DI water	2–4%	4%
	Time	3–5 min	5 min
Soft bake	Temperature, time	100–150 °C; 2–3 min	–
Etching	$FeCl_3$ in DI water	8–20%	15%
	Temperature	32–40 °C	35–40 °C
	Time	60–30 min	40 min

3.1. DFNPR Hardening and Development

The DFNPR showed strong resistance to most acid etching solutions and maintained stability within the pH range of 8.0–8.5 in alkaline environments. This confirmed its suitability for stable pattern transfer and chemical stability during subsequent etching. As shown in Figure 4a–c, we observed that both the pattern width and the exposure dose played significant roles in determining the quality of the hardened surface [39]. Wider patterns required a higher exposure dose to ensure complete cross-linking (polymerisation): when a wide feature received too low a dose, the resist was only partly cross-linked, adhered weakly to the copper, and was carried away in the developer, whereas doses of 100–120 mJ/cm^2 were sufficient for features up to about 85 µm. When the dose was raised to 180 mJ/cm^2, the photoresist hardened effectively, adhered firmly to the metal surface, and resisted dissolution during development, so these settings were used for the 250 µm traces of the devices. The DFNPR film thickness influenced the process. Thicker DFNPR layers required greater exposure energy to achieve uniform hardening across the depth, while thinner films hardened more easily but were comparatively less durable during development. Thus, exposure dose, film thickness, and pattern dimensions together governed the lithographic performance of DFNPR [40,41].

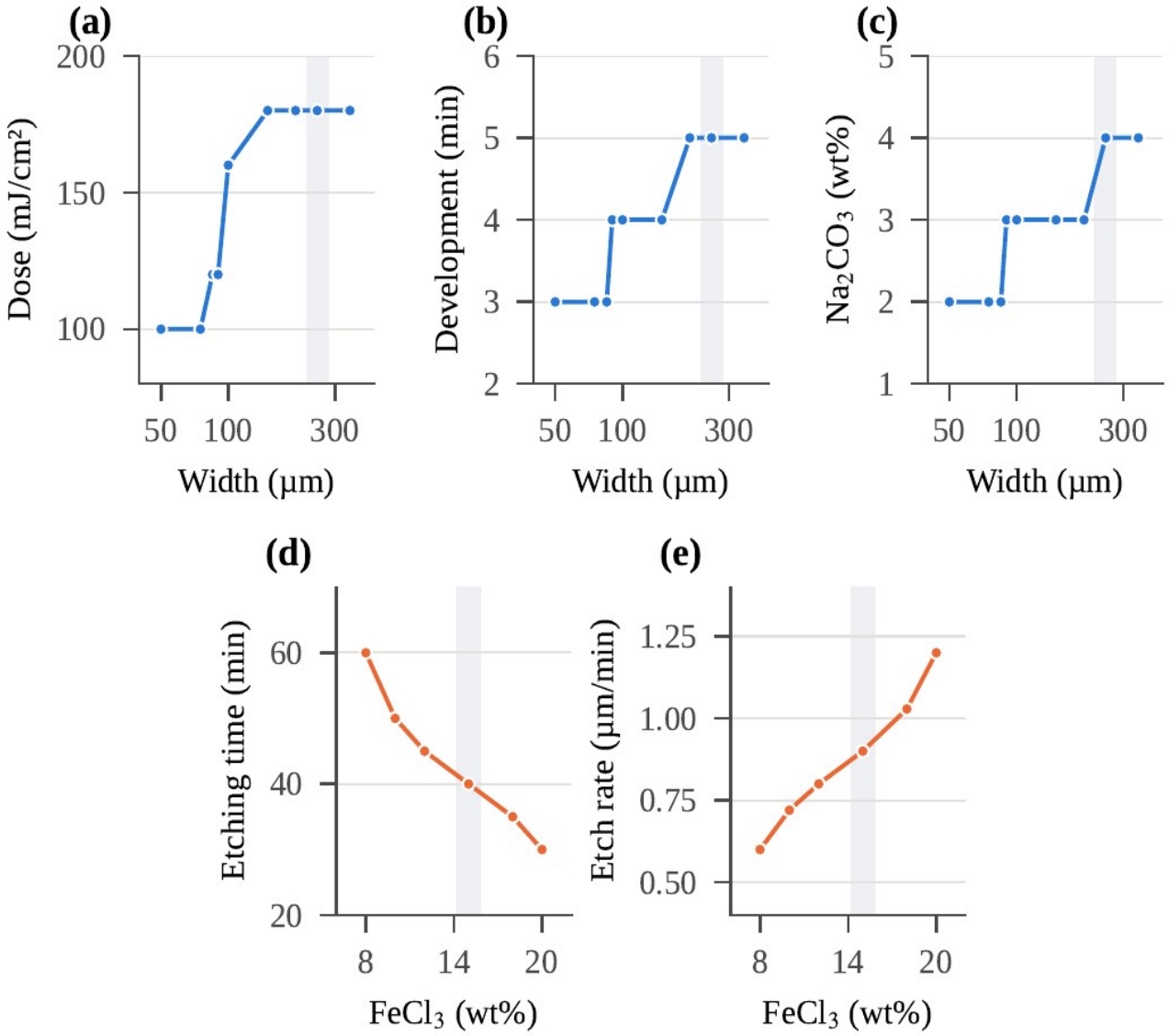

Figure 4. Process windows. Development: (**a**) exposure dose, (**b**) development time, and (**c**) Na_2CO_3 concentration used for each width of the developed resist features (365 nm exposure). Etching of the 36 µm copper foil at 32–40 °C: (**d**) etching time and (**e**) mean etch rate versus $FeCl_3$ concentration. Shaded: the settings used for the devices (250 µm features, 15% $FeCl_3$).

3.2. $FeCl_3$ Concentration Tuning

The chemical reaction between copper and the etchant ($FeCl_3$) was crucial, as different concentrations of etchants behaved uniquely during the chemical wet etching process. The reaction between copper (Cu) and ferric chloride ($FeCl_3$) proceeded as follows: $FeCl_3 + Cu \rightarrow FeCl_2 + CuCl$ [42,43].

The primary goal of chemical etching was to selectively remove unwanted copper from unexposed areas of DFNPR after development by Na_2CO_3, forming the desired interconnects and electrodes while achieving a smooth surface finish. For each experiment, 200 mL of etchant (prepared at a specified weight % with deionised water) was placed in a 20 cm × 10 cm × 5 cm tub or flask, where the sample was immersed. As shown in Figure 4d,e, the etching performance of $FeCl_3$ on copper (3M Copper Tape 1125, 0.036 mm thick) was influenced by several factors, including etchant concentration, temperature, and immersion time [44,45]. At 32–40 °C, the etching time decreased from 60 min at 8% $FeCl_3$ to 40 min at 15% and 30 min at 20% (diluted with DI water), and 15% for 40 min was used for the devices. Precision etching was critical, particularly when the copper interconnect was encapsulated or embedded by a stretchable substrate, as improper etching could damage the interface during device testing [46,47].

3.3. Area & Volume of the Device Component

The dimensions of a device component, with all measurements specified in millimetres (mm), are shown in Figure 5a. Associated pads have dimensions (W_p) of 4 mm and (L_p) of 7 mm. Specific patterns include a horseshoe width (W_h) of 0.35 mm in Figure 5b, and Figure 5c, which interconnects with 14 electrodes (N). Its overall dimensions are a total length (L) of 36.6 mm and a total width (W) of 12 mm. Individual electrodes have a thickness (t) of 0.036 mm, a side length (S_L) of 7 mm, and a side width (S_W) of 0.4 mm, with a horseshoe width (W_h) of 0.25 mm. The interspace between electrodes (S_i) is 0.55 mm. Based on a provided formula ($L \times W \times N + S_L \times S_W \times 2$), the calculated area is 6154.4 mm^2, leading to an estimated volume (Area × t) of 221.558 mm^3.

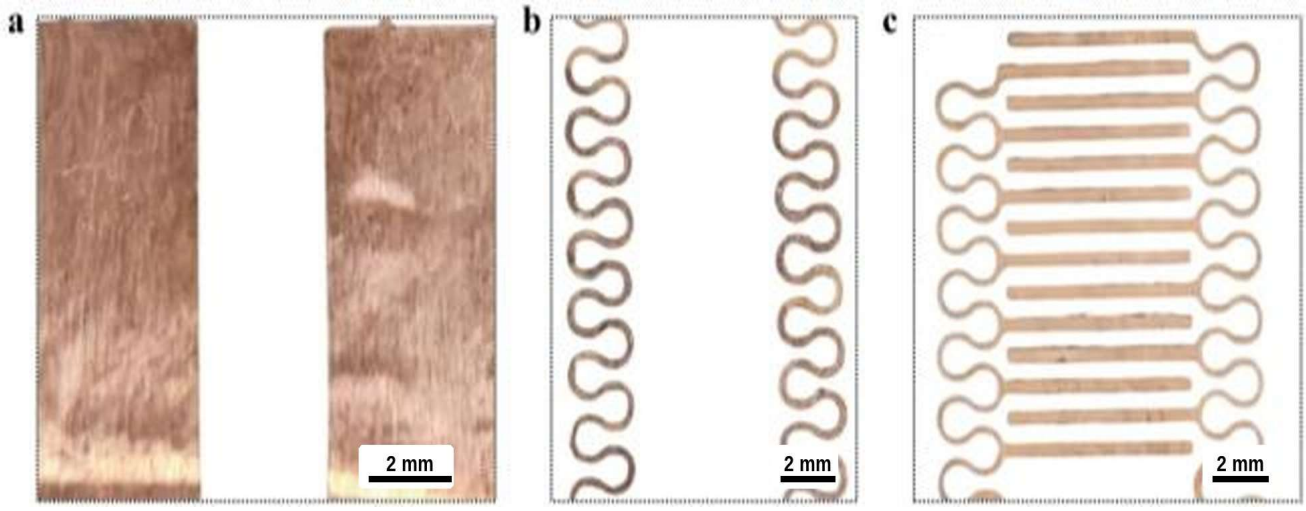

Figure 5. Post-etching of the pattern on the PDMS substrate, (**a**) Fabricated flexible sensing pad structure, (**b**) Horse-shaped interconnect design showing patterned conductive paths, (**c**) Final electrode integrated with a horse-shaped interconnect. Scale bars are calibrated from the mask dimensions (pad width 4 mm, horseshoe period 1.9 mm, finger pitch 0.95 mm).

3.4. Embedded Interconnect and Electrode

The images show optical microscopy of metallic traces microfabricated and embedded within the stretchable substrate. The fabrication process for creating embedded interconnects and electrodes on a PDMS substrate is shown in Figure 6a, beginning with the initial patterning of the etched pattern. In Figure 6b, unembedded copper follows these interconnects, and in Figure 6c, it is then fully embedded in the stretchable base to ensure mechanical stretchability and surface uniformity. In Figure 6d, the process concludes with the final, smoothly integrated structures, confirming successful encapsulation after curing.

The deformation and encapsulation behaviour of the embedded system is shown in Figure 6e,i, beginning with unstretched interconnects on the PDMS substrate, maintaining their original geometry. Figure 6f shows that these interconnects elongate uniformly upon stretching, demonstrating flexibility and mechanical stability. Similarly, unstretched electrodes encapsulated with a sensing composite, as shown in Figure 6g, have smooth alignment and a uniform coating. In Figure 6h, when placed under strain, they maintain their structural reliability and a consistent composite layer, confirming their suitability for stretchable sensing applications; their electromechanical response is quantified in Section 3.6.

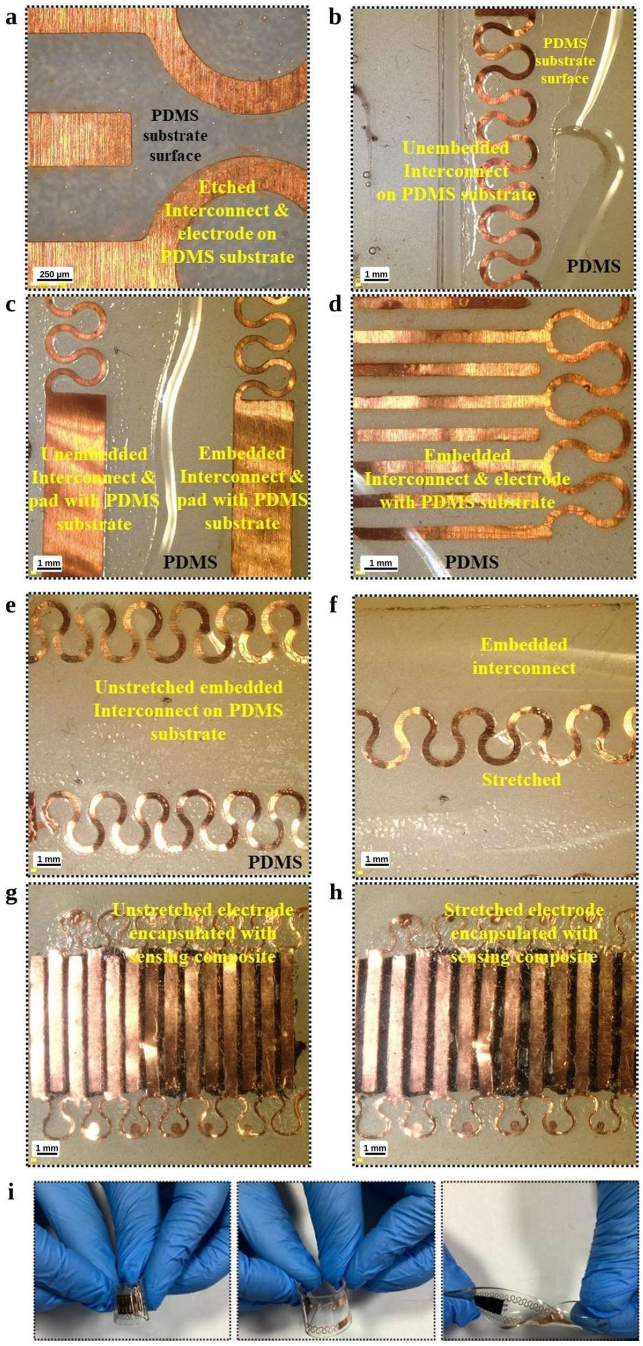

Figure 6. Embedded interconnects and electrodes in the PDMS substrate. (**a**–**d**): formation of unembedded and embedded structures: (**a**) etched interconnects and electrodes patterned on the PDMS substrate; (**b**) unembedded interconnects remain, showing the copper interconnect; (**c**) interconnects and pads embedded into the PDMS; (**d**) embedded structures showing successful encapsulation. (**e**–**h**): deformation and encapsulation behaviour: (**e**) unstretched embedded interconnects on the PDMS substrate; (**f**) stretched, the embedded interconnects elongate uniformly; (**g**) unstretched electrodes encapsulated with the sensing composite; (**h**) stretched, the encapsulated electrodes maintain structural reliability; (**i**) the device bending and twisting. Scale bars are calibrated from the mask dimensions.

3.5. Finite-Element Results

Under the 250 μm trace, the adhesive was compressed through its thickness up to 30% strain (median peel strain −0.07), and its peak peel strain stayed below 0.06. Under the 1 mm trace, it was pulled open: the peak peel strain was 0.14 at 20% and 0.20 at 30% strain, four to ten times higher, and the peak shear strain was 25–37% higher (Figure 7a,b). Narrowing the trace to 250 μm therefore reduces the opening load that drives debonding. Embedding also limits out-of-plane deformation: with the top PDMS, the copper

deflected 13 µm at 20% strain, below the foil thickness, but 49 µm without it (Figure 7c). The solution converged to 47.5% strain for the 250 µm trace and to 30% for the 1 mm trace. In the copper, plastic strain begins at about 1% applied strain and localises at the arc crowns of the horseshoe, reaching about 8% at 30% and 11% at 40% applied strain (Figure 7d–f), as in earlier simulations of horseshoe interconnects in PDMS [29,31]. The deformed traces show that, without the top PDMS, the trace rises and twists out of plane, whereas the embedded trace stays nearly flat (Figure 7g,h).

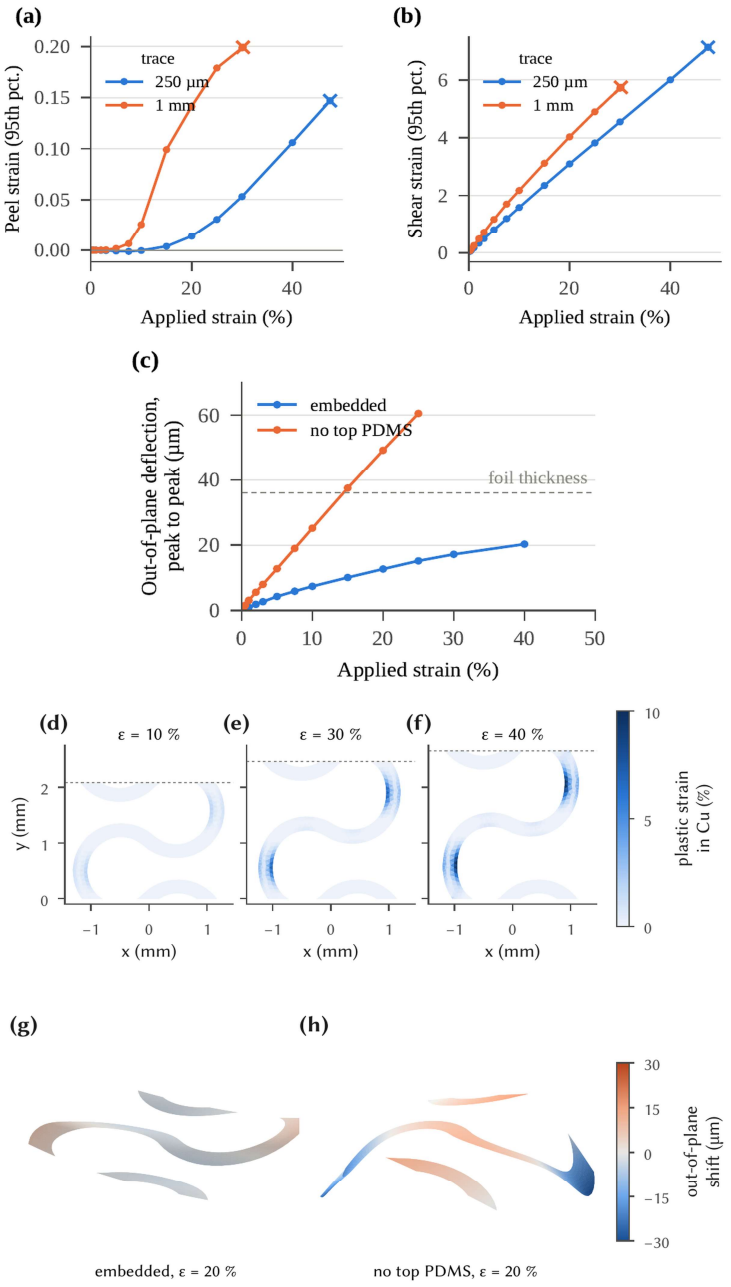

Figure 7. Finite-element results for one horseshoe period. (**a**) Peel and (**b**) shear strain in the adhesive under the copper (95th percentile) for the 250 µm trace and a 1 mm trace of the same shape (a cross marks loss of convergence); (**c**) peak-to-peak out-of-plane deflection of the 250 µm trace, embedded and without the top PDMS (10 µm initial imperfection); (**d**–**f**) equivalent plastic strain in the copper of the 250 µm trace at 10, 30 and 40% applied strain (dotted line: stretched period); (**g**,**h**) deformed copper trace at the same applied strain of 20%, (**g**) embedded and (**h**) without the top PDMS, coloured by the out-of-plane displacement relative to the mean plane of the trace (magnified 20 times; the colour span, about 11 and 47 µm, is the peak-to-peak deflection of (**c**)).

3.6. Electromechanical Response Under Cyclic Stretching

Both sensors started at 10.5 kΩ, and in both, the resistance nearly doubled during the first stretch (+91 and +87%, Figure 8a), a conditioning of the composite. Over cycles 4–23, the baseline resistance changed by −7% with the horseshoe interconnects, at a rate falling to −0.2% per cycle, but rose by 25% with straight leads and was still rising at +0.6% per cycle (Table 3). The early decrease with interconnects is a relaxation of the composite after conditioning: in a longer test of the same sensor, the baseline settled and then drifted slowly upward, by about +0.02% per cycle, thirty times less than with straight leads. With interconnects, the resistance–strain loops were repeatable (Figure 8c), more linear (R^2 0.66 versus 0.32) and less hysteretic (55 versus 133% of the span) than with straight leads (Figure 8d). The gauge factor was below 0.1 for both (Figure 8b, Table 3), so the interconnects improve the stability of the signal rather than its sensitivity, which is set by the composite. The sensor with straight leads needed a higher force for the same displacement (3.2 versus 1.9 N, Table 3), as the stiff strips concentrate the deformation in the composite between their ends. The force loops were unchanged between cycles 10 and 23, and neither sensor lost electrical continuity.

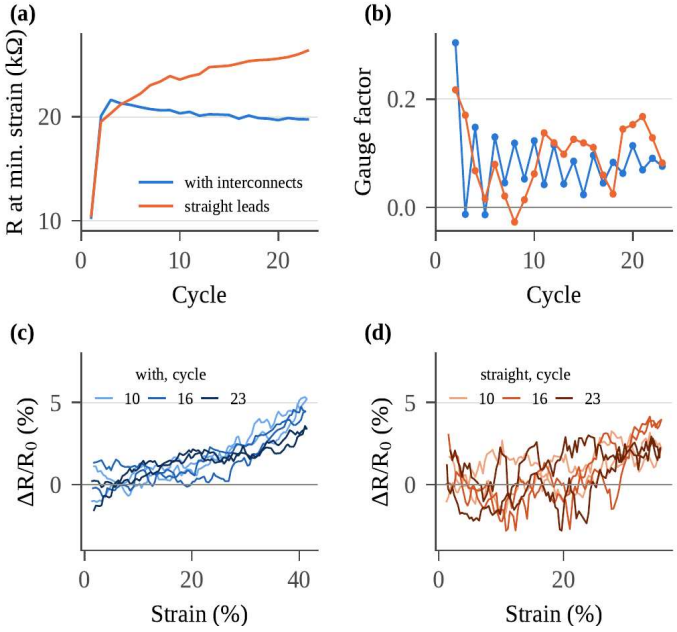

Figure 8. Cyclic tests of the two sensors over the same cycles: (**a**) resistance at minimum strain, (**b**) in-cycle gauge factor, (**c**,**d**) $\Delta R/R_0$ versus strain in cycles 10, 16 and 23 with horseshoe interconnects and with straight leads.

Table 3. Stability of the sensor response over cycles 4–23.

	With Interconnects	**Straight Leads**
Baseline drift (%)	−7.2	+24.5
Baseline coefficient of variation (%)	2.4	6.0
Gauge factor (median ± standard deviation)	0.08 ± 0.04	0.09 ± 0.05
Linearity R^2	0.66	0.32
Hysteresis (% of span)	55	133
Peak force (N)	1.95	3.21

3.7. Interrelation of the Results, Implications and Barriers

The results form one chain in which each step fixes the condition of the next. The process windows (Figure 4) show that the exposure dose and development time must grow with the feature width, so the width that can be patterned reliably in 36 µm foil is set by the lithography. The finite-element model then shows what that width means mechanically. The same horseshoe loads the adhesive in compression at 250

μm but pulls it open at 1 mm, and the top PDMS layer keeps the copper nearly flat, with a deflection of 13 μm against 49 μm at 20% strain. The sensor test shows the consequence at the device level. With the embedded horseshoe interconnects, the baseline stops drifting, while with straight leads it keeps rising. The three results are therefore not independent, since the trace width chosen in the process sets the adhesive load, and the load and the embedding together set the stability of the signal. The sensor comparison changes the interconnect shape, so on its own it cannot separate the effect of the horseshoe geometry from that of the width and of the embedding. This separation comes from the model, which is itself limited by an assumed adhesive modulus and does not model debonding.

For the wearable sector, two implications follow. First, interconnect design is part of the signal quality. The gauge factor was below 0.1 for both sensors, so the interconnects did not raise the sensitivity, but they removed a drift that would otherwise have to be corrected by repeated calibration on the body. Second, the route is accessible. Because it patterns commercial copper foil in place with maskless exposure and wet etching, a laboratory without vacuum equipment or a cleanroom can make interconnects that carry current in a 36 μm conductor, which a sub-micrometre film cannot.

The barriers are also clear from the same results. The 250 μm linewidth, set by the process window and by the 36 μm foil, limits the density of interconnects compared with thin-film routes. Direct writing took 20 min per device and the etching 40 min, so the route is serial and slow for production. The copper reaches 8–11% plastic strain at the arc crowns at 30–40% applied strain, so its fatigue life, which a 23-cycle test cannot show, has to be measured over thousands of cycles. The adhesion of the patterns was not measured, and the sensitivity of the composite remains the limit of the sensor. Addressing these four points (adhesion, throughput, fatigue life, and sensitivity) is what would take the approach from a demonstration to a wearable device.

4. Conclusions

This study demonstrates a photolithography process for creating copper interconnects on stretchable PDMS. By controlling the UV exposure, developer, and etchant parameters for each feature width, we achieved traces with a minimum linewidth of 250 μm in 36 μm copper foil, fully embedded in PDMS, without vacuum deposition, transfer, or a cleanroom. A finite-element model showed that the 250 μm traces keep the adhesive in compression up to 30% strain and that embedding reduces the out-of-plane deflection about fourfold. With the embedded horseshoe interconnects, the baseline of a strain sensor settled after a 7% relaxation and then drifted by only about +0.02% per cycle, against +25% over 20 cycles with straight leads, and the sensor responded more linearly and with less hysteresis, without electrical failure.

Taken together, the results show that the three stages of the work depend on each other. The process sets the trace width; the width and the embedding then set the load on the adhesive and the flatness of the copper, and these in turn set the stability of the signal. For wearable devices, this suggests that the interconnect, and not only the sensing material, determines whether a sensor can be read without repeated calibration, and that a laboratory with no vacuum equipment or cleanroom can make such interconnects. Several barriers remain before the route can be used in devices. These are the 250 μm minimum linewidth, the serial and slow patterning (about an hour per device), the unmeasured adhesion of the patterns, the unknown fatigue life of the copper beyond 23 cycles, and the low sensitivity of the composite. Our work provides a basis for advancing wearable devices and soft robotics. Further work will address these barriers, starting with peel testing of the adhesion and long-term cyclic tests.

Statement of the Use of Generative AI and AI-Assisted Technologies in the Writing Process

During the preparation of this manuscript, the authors used Grammarly in order to correct grammar. After using this tool, the authors reviewed and edited the content as needed and take full responsibility for the content of the published article.

Author Contributions

M.S.Y. designed the study, fabricated the devices, and wrote the manuscript; N.S. carried out the electromechanical testing; A.V. carried out the finite-element simulations; V.K.P. supervised the work and revised the manuscript.

Ethics Statement

Not applicable.

Informed Consent Statement

Not applicable.

Data Availability Statement

The data presented in this study are available on request from the corresponding author.

Funding

This research received no external funding.

Declaration of Competing Interest

The authors declare that they have no known competing financial interests or personal relationships that could have appeared to influence the work reported in this paper.

References

1. Hassan M, Abbas G, Li N, Afzal A, Haider Z, Ahmed S, et al. Significance of Flexible Substrates for Wearable and Implantable Devices: Recent Advances and Perspectives. *Adv. Mater. Technol.* **2022**, *7*, 2100773. DOI:10.1002/admt.202100773
2. Zhang Y, Zhang T, Huang Z, Yang J. A New Class of Electronic Devices Based on Flexible Porous Substrates. *Adv. Sci.* **2022**, *9*, 2105084. DOI:10.1002/advs.202105084
3. Liu Y, He K, Chen G, Leow WR, Chen X. Nature-Inspired Structural Materials for Flexible Electronic Devices. *Chem. Rev.* **2017**, *117*, 12893–12941. DOI:10.1021/acs.chemrev.7b00291
4. Rogers JA, Someya T, Huang Y. Materials and Mechanics for Stretchable Electronics. *Science* **2010**, *327*, 1603–1607. DOI:10.1126/science.1182383
5. Wu W. Stretchable electronics: Functional materials, fabrication strategies and applications. *Sci. Technol. Adv. Mater.* **2019**, *20*, 187–224. DOI:10.1080/14686996.2018.1549460
6. Guo X, Zhang Z, Ren Z, Li D, Xu C, Wang L, et al. Advances in Intelligent Nano-Micro-Scale Sensors and Actuators: Moving toward Self-Sustained Edge AI Microsystems. *Adv. Mater.* **2025**, *37*, e10417. DOI:10.1002/adma.202510417
7. Dong X, Luo X, Zhao H, Qiao C, Li J, Yi J, et al. Recent advances in biomimetic soft robotics: Fabrication approaches, driven strategies and applications. *Soft Matter* **2022**, *18*, 7699–7734. DOI:10.1039/d2sm01067d
8. Hou W, Liao Q, Xie S, Song Y, Qin L. Prospects and Challenges of Flexible Stretchable Electrodes for Electronics. *Coatings* **2022**, *12*, 558. DOI:10.3390/coatings12050558
9. Jung J, Kim KK, Suh YD, Hong S, Yeo J, Ko SH. Recent progress in controlled nano/micro cracking as an alternative nano-patterning method for functional applications. *Nanoscale Horiz.* **2020**, *5*, 1036–1049. DOI:10.1039/d0nh00241k
10. Cheng T, Zhang Y, Lai WY, Huang W. Stretchable Thin-Film Electrodes for Flexible Electronics with High Deformability and Stretchability. *Adv. Mater.* **2015**, *27*, 3349–3376. DOI:10.1002/adma.201405864

11. Wang B, Facchetti A. Mechanically Flexible Conductors for Stretchable and Wearable E-Skin and E-Textile Devices. *Adv. Mater.* **2019**, *31*, 1901408. DOI:10.1002/adma.201901408
12. Kim M, Kim DJ, Ha D, Kim T. Cracking-assisted fabrication of nanoscale patterns for micro/nanotechnological applications. *Nanoscale* **2016**, *8*, 9461–9479. DOI:10.1039/c5nr06266g
13. Chen PY, Liu M, Wang Z, Hurt RH, Wong IY. From Flatland to Spaceland: Higher Dimensional Patterning with Two-Dimensional Materials. *Adv. Mater.* **2017**, *29*, 1605096. DOI:10.1002/adma.201605096
14. Morales-Masis M, De Wolf S, Woods-Robinson R, Ager JW, Ballif C. Transparent Electrodes for Efficient Optoelectronics. *Adv. Electron. Mater.* **2017**, *3*, 1600529. DOI:10.1002/aelm.201600529
15. Won D, Bang J, Choi SH, Pyun KR, Jeong S, Lee Y, et al. Transparent Electronics for Wearable Electronics Application. *Chem. Rev.* **2023**, *123*, 9982–10078. DOI:10.1021/acs.chemrev.3c00139
16. Pease RF, Chou SY. Lithography and Other Patterning Techniques for Future Electronics. *Proc. IEEE* **2008**, *96*, 248–270. DOI:10.1109/jproc.2007.911853
17. Pimpin A, Srituravanich W. Review on Micro- and Nanolithography Techniques and their Applications. *Eng. J.* **2012**, *16*, 37. DOI:10.4186/ej.2012.16.1.37
18. Sharma E, Rathi R, Misharwal J, Sinhmar B, Kumari S, Dalal J, et al. Evolution in Lithography Techniques: Microlithography to Nanolithography. *Nanomaterials* **2022**, *12*, 2754. DOI:10.3390/nano12162754
19. Park CW, Moon YG, Seong H, Jung SW, Oh JY, Na BS, et al. Photolithography-Based Patterning of Liquid Metal Interconnects for Monolithically Integrated Stretchable Circuits. *ACS Appl. Mater. Interfaces* **2016**, *8*, 15459–15465. DOI:10.1021/acsami.6b01896
20. Cho D, Park J, Kim T, Jeon S. Recent advances in lithographic fabrication of micro-/nanostructured polydimethylsiloxanes and their soft electronic applications. *J. Semicond.* **2019**, *40*, 111605. DOI:10.1088/1674-4926/40/11/111605
21. Lacour SP, Wagner S, Huang Z, Suo Z. Stretchable gold conductors on elastomeric substrates. *Appl. Phys. Lett.* **2003**, *82*, 2404–2406. DOI:10.1063/1.1565683
22. Gray DS, Tien J, Chen CS. High-Conductivity Elastomeric Electronics. *Adv. Mater.* **2004**, *16*, 393–397. DOI:10.1002/adma.200306107
23. Verplancke R, Bossuyt F, Cuypers D, Vanfleteren J. Thin-film stretchable electronics technology based on meandering interconnections: Fabrication and mechanical performance. *J. Micromech. Microeng.* **2012**, *22*, 015002. DOI:10.1088/0960-1317/22/1/015002
24. Linghu C, Zhang S, Wang C, Song J. Transfer printing techniques for flexible and stretchable inorganic electronics. *npj Flex. Electron.* **2018**, *2*, 26. DOI:10.1038/s41528-018-0037-x
25. Kim DH, Ahn JH, Choi WM, Kim HS, Kim TH, Song J, et al. Stretchable and Foldable Silicon Integrated Circuits. *Science* **2008**, *320*, 507–511. DOI:10.1126/science.1154367
26. Matsuhisa N, Kaltenbrunner M, Yokota T, Jinno H, Kuribara K, Sekitani T, et al. Printable elastic conductors with a high conductivity for electronic textile applications. *Nat. Commun.* **2015**, *6*, 7461. DOI:10.1038/ncomms8461
27. Dickey MD. Stretchable and Soft Electronics using Liquid Metals. *Adv. Mater.* **2017**, *29*, 1606425. DOI:10.1002/adma.201606425
28. Brosteaux D, Axisa F, Gonzalez M, Vanfleteren J. Design and Fabrication of Elastic Interconnections for Stretchable Electronic Circuits. *IEEE Electron Device Lett.* **2007**, *28*, 552–554. DOI:10.1109/led.2007.897887
29. Gonzalez M, Axisa F, Vanden Bulcke M, Brosteaux D, Vandevelde B, Vanfleteren J. Design of metal interconnects for stretchable electronic circuits. *Microelectron. Reliab.* **2008**, *48*, 825–832. DOI:10.1016/j.microrel.2008.03.025
30. Vanfleteren J, Gonzalez M, Bossuyt F, Hsu YY, Vervust T, De Wolf I, et al. Printed circuit board technology inspired stretchable circuits. *MRS Bull.* **2012**, *37*, 254–260. DOI:10.1557/mrs.2012.48
31. Patidar D, Pal VK. Deformation behaviour of interconnect encapsulated on functionally graded stretchable substrates. *Int. J. Mech. Sci.* **2023**, *257*, 108539. DOI:10.1016/j.ijmecsci.2023.108539
32. Patidar D, Bhasin A, Pal VK. Experimental and numerical investigation on reliability of encapsulated sine wave interconnect for stretchable substrates. *Microelectron. Reliab.* **2024**, *155*, 115355. DOI:10.1016/j.microrel.2024.115355
33. Nalamasu O, Cheng M, Timko AG, Pol V, Reichmanis E, Thompson LF. An overview of resist processing for deep-UV lithography. *J. Photopolym. Sci. Technol.* **1991**, *4*, 299–318. DOI:10.2494/photopolymer.4.299
34. Dong Z, He Q, Shen D, Gong Z, Zhang D, Zhang W, et al. Microfabrication of functional polyimide films and microstructures for flexible MEMS applications. *Microsyst. Nanoeng.* **2023**, *9*, 31. DOI:10.1038/s41378-023-00503-5
35. Roos MM, Winkler A, Nilsen M, Menzel SB, Strehle S. Towards Green 3D-Microfabrication of Bio-MEMS Devices Using ADEX Dry Film Photoresists. *Int. J. Precis. Eng. Manuf. Green Technol.* **2022**, *9*, 43–57. DOI:10.1007/s40684-021-00367-y
36. Zhang M, Meng F, Li X, Zeng W. Applications of Dry Film Photoresist in Micromachining: A Review. *Micromachines* **2025**, *16*, 1258. DOI:10.3390/mi16111258

37. Zeb G, Duong XT, Vu NP, Phan QT, Nguyen DT, Ly VA, et al. Chemical metallization of KMPR photoresist polymer in aqueous solutions. *Appl. Surf. Sci.* **2017**, *407*, 518–525. DOI:10.1016/j.apsusc.2017.02.231
38. Nilsen M, Port F, Roos M, Gottschalk KE, Strehle S. Facile modification of freestanding silicon nitride microcantilever beams by dry film photoresist lithography. *J. Micromech. Microeng.* **2019**, *29*, 025014. DOI:10.1088/1361-6439/aaf7e3
39. Otoguro A, Kuboyama T, Onishi O. Novel Low D_f Photosensitive Materials for Redistribution Layer. *J. Photopolym. Sci. Technol.* **2024**, *37*, 481–484. DOI:10.2494/photopolymer.37.481
40. Martínez ED, Prado A, Gonzalez M, Anguiano S, Tosi L, Salazar Alarcón L, et al. Recent Advances on Nanocomposite Resists with Design Functionality for Lithographic Microfabrication. *Front. Mater.* **2021**, *8*, 629792. DOI:10.3389/fmats.2021.629792
41. Liu G, Petrosko SH, Zheng Z, Mirkin CA. Evolution of Dip-Pen Nanolithography (DPN): From Molecular Patterning to Materials Discovery. *Chem. Rev.* **2020**, *120*, 6009–6047. DOI:10.1021/acs.chemrev.9b00725
42. Wang Z, Che J, Ye C. Application of ferric chloride both as oxidant and complexant to enhance the dissolution of metallic copper. *Hydrometallurgy* **2010**, *105*, 69–74. DOI:10.1016/j.hydromet.2010.07.013
43. Al-Harahsheh M, Kingman S, Al-Harahsheh A. Ferric chloride leaching of chalcopyrite: Synergetic effect of $CuCl_2$. *Hydrometallurgy* **2008**, *91*, 89–97. DOI:10.1016/j.hydromet.2007.11.011
44. Patil D, Thorat S, Sadaiah M. Study of the effect of PCM process parameters on geometry type, Ra, depth of etch, undercut comparing $FeCl_3$ and $CuCl_2$ etchants on Monel 400. *Adv. Mater. Process. Technol.* **2024**, *10*, 1956–1976. DOI:10.1080/2374068X.2023.2205668
45. Cakir O. Photochemical Machining of Brass with Cupric Chloride Etchants. Ph.D. Thesis, Cranfield University, Cranfield, UK, 1996. Available online: http://hdl.handle.net/1826/3623 (accessed on 31 October 2026).
46. Yadav RS, Jadhav TA, Gadekar T, Patil V, Purandare P, Kulkarni A, et al. Experimental study on parameter evaluation of thin metal sheets using photochemical machining. *J. Integr. Sci. Technol.* **2025**, *13*, 1119. DOI:10.62110/sciencein.jist.2025.v13.1119
47. Dahiya AS, Christou A, Ma S, Dahiya R. Printed Interconnects for Heterogeneous Systems Integration on Flexible Substrates. *Adv. Mater. Technol.* **2025**, *10*, 2401213. DOI:10.1002/admt.202401213